PASJ: Publ. Astron. Soc. Japan **55**, 967–980, 2003 October 25
© 2003. Astronomical Society of Japan.

Hydrodynamic Modeling of a Flare Loop Connecting the Accretion Disk and Central Core of Young Stellar Objects

Hiroaki ISOBE and Kazunari SHIBATA
Kwasan and Hida Observatories, Kyoto University, Yamashina, Kyoto 607-8471
isobe@kwasan.kyoto-u.ac.jp
Takaaki YOKOYAMA
Department of Earth and Planetary Science, The University of Tokyo, 7-3-1 Hongo, Bunkyo-ku, Tokyo 113-0033
Nobeyama Radio Observatory, Nobeyama, Minamimaki, Minamisaku, Nagano 384-1305
and
Kensuke IMANISHI
Department of Physics, Graduate School of Science, Kyoto University, Sakyo-ku, Kyoto 606-8502

(Received 2002 October 23; accepted 2003 July 11)

Abstract

Many young stellar objects, such as protostars and T-Tauri stars, show strong flare activity. In this paper we present a hydrodynamic simulation of a flare loop that connects the central star and the accretion disk, and discuss the evaporation of the chromosphere of the central star and the disk. We assumed a long ($> 10\,R_\odot$) loop length, and that the flare energy is deposited near the half-way point between the disk and the stellar surface. We found that in some cases all of the plasma in the accretion disk is heated to the flare temperature and spreads over the flare loop. The condition for this "disk disappearance" was examined. The X-ray spectrum expected when we *observe* the simulation result was synthesized by taking into account the instrumental response of ASCA/GIS. However, we could not find any clear observational signature of the existence of the disk, because the bulk properties of a flare loop are determined by the flare heating flux and loop length, and not by the involvement of the disk. We found that the synthesized spectrum is reasonably fitted with a two-temperature model, and that the temperature of the hotter component is several factors lower than the maximum temperature of the simulation result.

Key words: hydrodynamics — stars: flare — stars: pre-main sequence — X-rays: stars

1. Introduction

X-ray observations during the last decade have revealed that young stellar objects (YSOs), such as protostars and T-Tauri stars, are strong X-ray emitters. A flare-like time variability has also been observed (e.g., Koyama et al. 1994, 1996; Kamata et al. 1997; Grosso et al. 1997; Ozawa et al. 1999; Tsuboi et al. 2000; see Feigelson, Montmerle 1999 for a review). In analogy to solar flares, these YSO flares are believed to be produced by magnetic activity. However, the physical parameters of protostellar flares are different from those of solar flares. For instance, the total energy over the full X-ray band is 10^{34-36} erg, while the total energy released in solar flares is typically 10^{29-32} erg. Also, the spectrum of a protostellar flare is harder than that of solar flares, which indicates the existence of 8–10 keV plasma.

One plausible scenario for the YSO flares is interactions of the magnetic field lines that connect the central star and the accretion disk (e.g., Shu et al. 1987; Hayashi et al. 1996; Montmerle et al. 2000). Hayashi, Shibata, and Matsumoto (1996) performed a 2.5-dimensional MHD simulation of the magnetic interaction in the magnetosphere of a protostar. Their model consists of a dipole magnetic field connecting the star and the disk. Because the magnetic loops are twisted by the differential rotation of the star and the disk, the loops expand and a current sheet is formed. In the presence of resistivity, magnetic reconnection occurs, leading to strong plasma heating and mass ejection. Although these processes seem to be very likely to occur if the magnetic field directly connects the star and the disk, the actual magnetic geometry in YSOs is still controversial. Since spatially resolved observation of flares in stellar coronae has not been achieved, realistic numerical modeling of flare loops is necessary to derive the physical parameters from the observed X-ray light curves and spectra.

In solar flares, the magnetic energy in the corona is converted into the thermal energy of hot ($\sim 10^7$ K) plasma via magnetic reconnection. The released energy heats the cool ($\sim 10^4$ K) plasma in the chromosphere by heat conduction or non-thermal particles; then, the heated chromospheric plasma is evaporated into the corona and fills the closed flare loop. This process, chromospheric evaporation, increases the emission measure and hence the X-ray luminosity. Therefore, heat conduction and evaporation of the chromosphere of the star and the disk must be taken into account for any realistic modeling of X-ray observation. Hori et al. (1997) carried out a pseudo two-dimensional hydrodynamic simulation of a solar flare, including heat conduction and chromospheric evaporation. Their result well reproduced the soft X-ray observation of Yohkoh. More recently, Reeves and Warren (2002) made a model of the cooling of postflare loops, and found that the multi-loop model can fit the observed light curves better than the single-loop model. Two-dimensional MHD simulation with anisotropic heat conduction and chromospheric evaporation was performed by Yokoyama and Shibata (1998, 2001).

One-dimensional hydrodynamic modelings of solar-flare loops and its extension to stellar flares have been done extensively (e.g., Reale et al. 1997; Reale, Micela 1998). However, previous studies have considered flares on the stellar surface. In this paper, we present the one-dimensional hydrodynamic simulation of a flare loop connecting the star and the disk, with particular emphasis on evaporation of the disk. The preliminary result has been presented by Isobe, Yokoyama, and Shibata (2001). In section 2 we describe the numerical model. Numerical results are shown in section 3, and in section 4 we discuss the results.

2. Numerical Model

2.1. Fundamental Assumptions and Basic Equations

The model consists of a rigid magnetic loop that penetrates the accretion disk with both ends anchored in the photosphere of the central star. Figure 1 schematically illustrates the model. The geometry of the loop is assumed to be semi-circular with a constant cross section. The mass and radius of the central star are set to be $1\,M_\odot$ and $4\,R_\odot$, respectively. For simplicity we assume that the fluid is hydrogen plasma, and use a single-fluid description, i.e., ions and electrons have the same temperature and bulk velocities. Other elements are included in evaluating the radiative losses.

We calculate the dynamics of magnetically confined plasma in the loop using a one-dimensional hydrodynamic code. The basic equations are:

$$\frac{\partial \rho}{\partial t} + \frac{\partial}{\partial s}(\rho v) = 0, \tag{1}$$

$$\frac{\partial \rho v}{\partial t} + \frac{\partial}{\partial s}(\rho v^2) = -\rho g_{\parallel} - \frac{\partial P}{\partial s}, \tag{2}$$

$$\frac{\partial E}{\partial t} + \frac{\partial}{\partial s}[(E + P)v] = \frac{\partial}{\partial s}\left(\kappa_{\parallel}\frac{\partial T}{\partial s}\right) - \rho g_{\parallel} v - R + H, \tag{3}$$

where

$$P = 2nk_{\rm B}T, \quad E = \frac{1}{2}\rho v^2 + \frac{P}{\gamma - 1}. \tag{4}$$

Here, s is the distance along the loop from the photosphere on the central star, and $g_{\parallel}$ is the acceleration by the gravity of the central star along the loop. The gravity of the disk and the effect of rotation are not taken into account. The other parameters have their usual meanings. γ is the ratio of the specific heats, and is set to be 5/3. The radiative loss function, $R = n^2 Q(T)$, is chosen to approximate the form for a plasma with normal solar abundances; $Q(T)$ is shown in figure 2. The thermal conductivity is assumed to be of the classical Spitzer form (Spitzer 1962), that is, $\kappa_{\parallel} = \kappa_0 T^{5/2}\,{\rm erg\,s^{-1}\,cm^{-1}\,K^{-1}}$ and $\kappa_0 = 10^{-6}$ in cgs units. The resulting heat flow is assumed not to be flux-limited. The heating function H is given by $H(s,t) = H_{\rm q}(s) + H_{\rm f}(s,t)$. The static heating term $H_{\rm q}(s)$ is assumed to balance the radiative losses in the initial condition at each point. The second term $H_{\rm f}(s,t)$ is the flare heating, which is described later.

The variables are normalized by the values in the photosphere at the initial state. The normalization units are summarized in table 1.

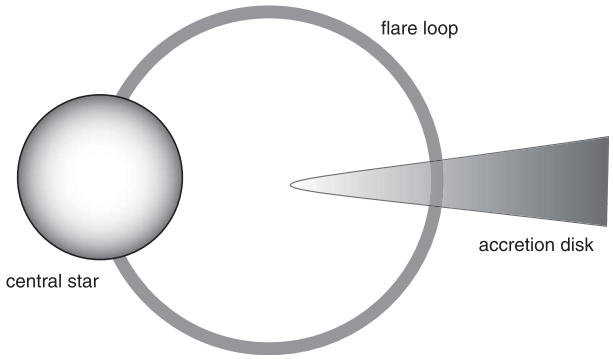

Fig. 1. Schematic picture of a flare loop connecting the central star and the accretion disk.

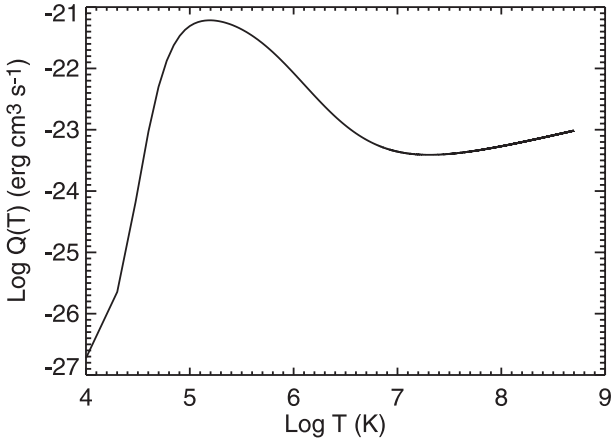

Fig. 2. Radiative loss function $Q(T)$.

2.2. Initial Conditions and Flare Parameters

The initial temperature distribution is assumed to be

$$T = \begin{cases} T_{\rm pho} + \dfrac{T_{\rm cor} - T_{\rm pho}}{2}\left[\tanh\left(\dfrac{s - s_{\rm tr,star}}{w_{\rm tr}}\right) + 1\right] \\ \qquad\qquad \left(0 \le s \le \dfrac{L}{2}\right) \\ T_{\rm dis} + \dfrac{T_{\rm cor} - T_{\rm dis}}{2}\left[\tanh\left(\dfrac{-s + s_{\rm tr,disk}}{w_{\rm tr}}\right) + 1\right] \\ \qquad\qquad \left(\dfrac{L}{2} \le s \le L\right), \end{cases} \tag{5}$$

and is symmetric for $L < s \le 2L$, where $2L$ is the total loop length. We adopt $2L = 9.8 \times 10^{11}\,{\rm cm} \approx 14\,R_\odot$, which was derived for the quasi-periodic flares in YLW 15 using a quasi-static method (Tsuboi et al. 2000). The photospheric temperature $T_{\rm pho}$, the coronal temperature $T_{\rm cor}$, and the disk temperature $T_{\rm dis}$ are set to be $T_{\rm pho} = 10^4\,{\rm K}$, $T_{\rm cor} = 2 \times 10^6\,{\rm K}$, and $T_{\rm dis} = 10^4\,{\rm K}$, respectively. The locations of the transition regions are set to be $s_{\rm tr,star} = 4.48 \times 10^9\,{\rm cm}$ and $s_{\rm tr,disk} = L - 2.24 \times 10^{10}\,{\rm cm}$. Hence, the thickness of the disk $H_{\rm d}$ is $\sim 4.48 \times 10^{10}\,{\rm cm}$. The width of the transition region $w_{\rm tr}$ is set to be $1.6 \times 10^8\,{\rm cm}$.

The density and pressure distributions are calculated from the temperature distribution assuming hydrostatic equilibrium.

Table 1. Units for normalization.

Physical quantity	Normalization unit	Typical value
Temperature, T	$T_{\rm pho}$	$10^4\,{\rm K}$
Number density, n	$n_{\rm pho}$	$10^{17}\,{\rm cm^{-3}}$
Length, s	$h_{\rm pho} = k_{\rm B}T_{\rm pho}/mg_{\rm pho}$	$3.2\times10^3\,{\rm km}$
Velocity, v	$C_{\rm s,pho} = [\gamma k_{\rm B}T_{\rm pho}/m]^{1/2}$	$11.7\,{\rm km\,s^{-1}}$
Time, T	$h_{\rm pho}/C_{\rm s,pho}$	273 s
Density, ρ	$mn_{\rm pho}$	$1.7\times10^{-7}\,{\rm g\,cm^{-3}}$
Pressure, p	$\gamma n_{\rm pho}k_{\rm B}T_{\rm pho}$	$2.3\times10^5\,{\rm dyn\,cm^{-2}}$

Figure 3 shows the initial distribution of the temperature, number density, and pressure. The left column shows the distributions in the whole loop, and the right column shows those near the transition region. Since we assume that the static heating balances only the radiative loss, the initial condition is not in strict energy equilibrium. Therefore, a slight decrease of the coronal temperature and weak evaporation of the chromosphere and the disk spontaneously occur due to the conductive heat flux from the hot corona to the cold chromosphere/disk. However, they have negligible effects on the result of the simulation because the temperature increase and resultant evaporation by the flare are much stronger.

The flare heating function $H_{\rm f}(s,t)$ is of the form of spatially Gaussian,

$$H_{\rm f}(s,t) = F(t)\frac{1}{\sqrt{2\pi}\sigma}\exp\left[-\frac{(s-s_{\rm flr})^2}{2\sigma^2}\right]\ ({\rm erg\,cm^{-3}\,s^{-1}}). \quad (6)$$

We adopt $\sigma = 9.6\times10^4\,{\rm km}$ and $s_{\rm flr} = L/2$, i.e., the flare energy is deposited near the half-way point between the disk and the stellar surface, which is consistent with a two-dimensional MHD simulation (Hayashi et al. 1996). The total heat flux for the loop $F(t)$ is kept constant for $0 \le t \le t_{\rm f}$, and $F(t) = 0$ for $t_{\rm f} < t$. The duration time of flare heating $t_{\rm f}$ is assumed to be 12 normalized units = 3276 s. This is a reasonable value of the Alfvén transit time (and hence the heating duration time) of the loop if the coronal Alfvén speed is comparable to that of the solar corona, i.e., a few thousand $\rm km\,s^{-1}$.

2.3. *Numerical Algorithms*

The numerical algorithms are basically the same as those of Hori et al. (1997). We apply the time-splitting method (e.g., Choe, Lee 1992) to the energy equation (3) and integrate the hydrodynamic part, the heating and cooling parts, and the conduction part successively with different methods. Other equations are ideal hydrodynamic equations. We use a modified Lax–Wendroff method (Rubin, Burkstein 1967) for the hydrodynamic parts and adopt the successive overrelaxation (SOR) method for the heat conduction (e.g., Hirsch 1988). The boundary condition is a symmetric condition at both ends of the loop; the mass and energy fluxes across the boundaries vanish. We confirmed that the boundary condition does not affect the evolution of the flaring coronal loop because the conductive energy flux from flaring corona does not reach the boundary, which is deep below the dense chromosphere.

We used nonuniform grids, since we need more spatial resolution in the transition regions near the star and the disk, where the physical quantities drastically change. The grid size Δs smoothly decreases from 0.16 at the photosphere to 0.1 around the transition region of the star. In the corona, Δs increases from 0.1 to 10.0 and then decreases again to 0.02 outside the disk transition region. $\Delta s = 0.02$ through the disk transition region and the disk. The grid spacing is symmetric for $L < s < 2L$. The total grid number is 3094 for the case of $2L = 9.8\times10^{11}\,{\rm cm}$.

3. Numerical Results

3.1. *Case A: $F = 7.9\times10^9$ (erg cm^{-2} s^{-1})*

Figures 4–6 illustrate the distribution of the temperature (upper panels), number density (middle panels), and velocity (lower panels) in a case of $F = 7.9\times10^9$ ($\rm erg\,cm^{-2}\,s^{-1}$). The left column shows the distributions in the whole loop, and the right column shows those near the accretion disk. The dashed, dash-dotted, and solid lines show plots for different times. The plotted times are the same in each column, and indicated in the upper panels. The dotted lines show the initial conditions.

In figure 4 (t = 0–327 s), the high-temperature region of the flare rapidly spreads due to heat conduction. Weak flows toward the star and the disk follow the conduction fronts. The conduction front reaches the disk at t = 327 s, and hence the beginning of evaporation is seen in the density and velocity distribution. The density in the corona does not change in this phase.

In figure 5 (t = 546–2184 s) the conduction fronts impinge on the chromosphere and the disk, where plasmas are rapidly heated to the flare temperature. The resultant high pressure causes evaporation of the plasma both in the chromoshere and the disk. The velocity of the evaporation flow is about $800\,{\rm km\,s^{-1}}$ at most. Though the flare heating still continues in this phase, the temperature in the corona almost remained constant. The evaporation flows from the star and the disk collide near the loop summit, resulting in a slight increase in the temperature and the density. The flare loop is filled with hot ($T > 10^7\,{\rm K}$) and dense ($n \sim 10^{10}\,{\rm cm^{-3}}$) plasma.

Figure 6 shows the distributions after the flare heating stopped at t = 3276 s. As the temperature of the flare loop decreases, the evaporation flows become weak and hence the density increase in the flare loop slows down. The conduction front is stopped in the disk because of the low temperature and high density. The other side of the loop, i.e., beyond the disk, is not affected by the flare.

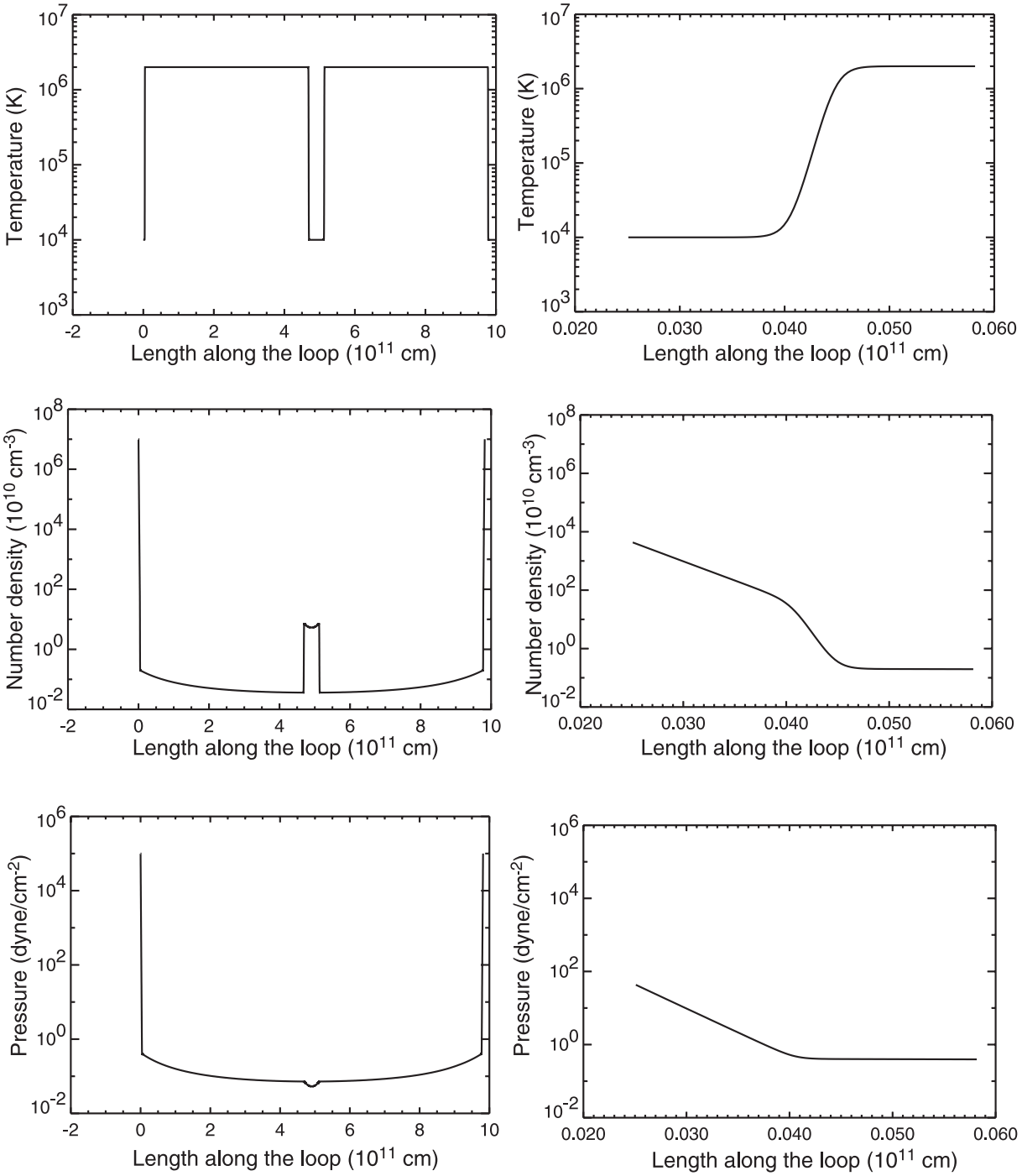

Fig. 3. Initial temperature (top panels), number density (middle panels), and pressure (bottom panels) distributions. The left panels show the whole loop, and the right panels show the vicinity of the transition region of the chromosphere of the star. The cool and dense parts in the middle represent the accretion disk.

Figure 7 shows the temporal variations of the maximum temperature in the loop (thick solid line), emission measure *EM* (thin solid line), and the distance between the two conduction fronts (dotted line). The emission measure *EM* is calculated as

$$EM = \int A n_5^2 \, ds, \tag{7}$$

where n_5 is the number density of the plasma with $T > 5\,\mathrm{MK}$. A is the cross section of the loop, assumed to be $3 \times 10^{22}\,\mathrm{cm}^2$. The distance between the conduction fronts is calculated as the length of the region where $T > 10\,\mathrm{MK}$. The temporal behavior of the maximum temperature and the distance between the conduction fronts is very similar in the first phase ($t < 2000\,\mathrm{s}$). This indicates that the maximum temperature is determined by the balance between the flare heating and the conductive

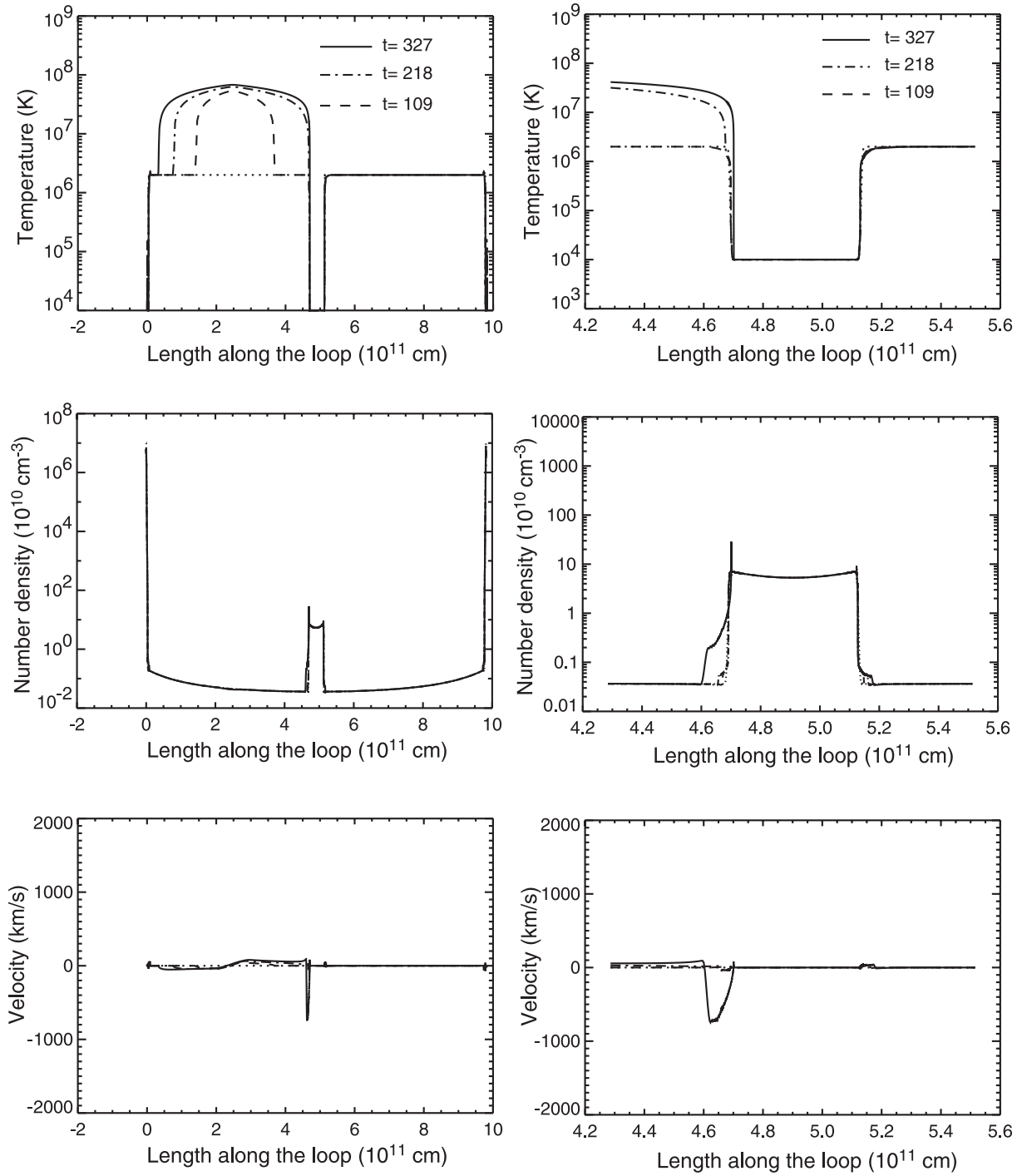

Fig. 4. Temperature (upper panels), number density (middle panels), and velocity (lower panels) distributions at t = 109, 218, and 327 s in case A. The left column shows the distributions of the whole loop, and the right column shows those near the disk. The dashed, dash-dotted, and solid lines show plots for different times, which are indicated in the upper panels. The dotted lines show the initial condition.

cooling. The slight increase in the temperature at $t \sim 2000$ s is because of the collision of the evaporation flows near the loop summit.

3.2. *Case B: $F = 7.9 \times 10^{10}$ (erg cm^{-2} s^{-1})*

Figures 8–10 show the result for a case with $F = 7.9 \times 10^{10}$ (erg cm^{-2} s^{-1}). In this case, the temperature is higher ($> 10^8$ K), and hence the conduction front propagates much faster than in case A (figure 8). Because of the larger heat flux into the chromosphere and the disk, the velocity and mass flux of the evaporation flows are also larger. The maximum velocity is more than 2000 km s^{-1}. Therefore, the conduction front, which is stopped in the disk in case A, penetrates the disk (figure 9). After the conduction front rapidly reaches the other

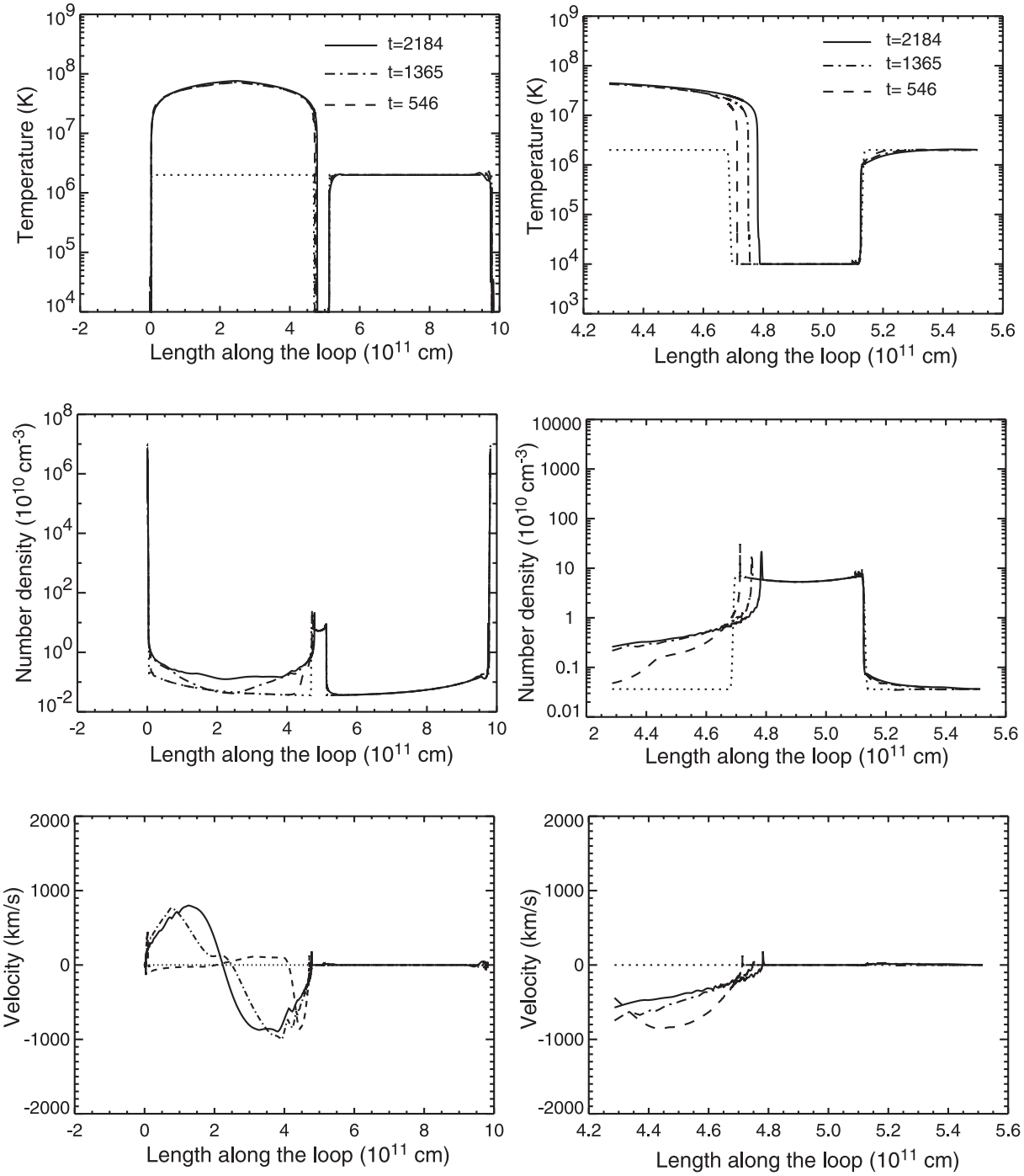

Fig. 5. Result for case A, t = 546, 1365, and 2184 s.

end of the loop, that is, the chromosphere of the star, evaporation from this side also occurs, filling the whole loop with hot plasma (figure 10). As a consequence, all of the plasma in the disk reached the flare temperature, and spreads over the loop, i.e., the accretion disk disappears. In subsection 4.2 we examine the condition in which disk disappearance occurs.

The temporal variations of the maximum temperature, *EM*, and the distance between the conduction fronts are shown in the lower left panel of figure 7. The temperature increase around t = 800 is due to the collision of strong evaporation flows from the star and the disk. After the conduction front penetrates the disk at t = 2000, the temperature increases again because conduction cooling becomes less effective, and *EM* increases due to the evaporation from the other end of the loop. However, differences in the temporal behaviors of temperature and *EM* between case A and case B are probably not distinguishable by the present X-ray observation.

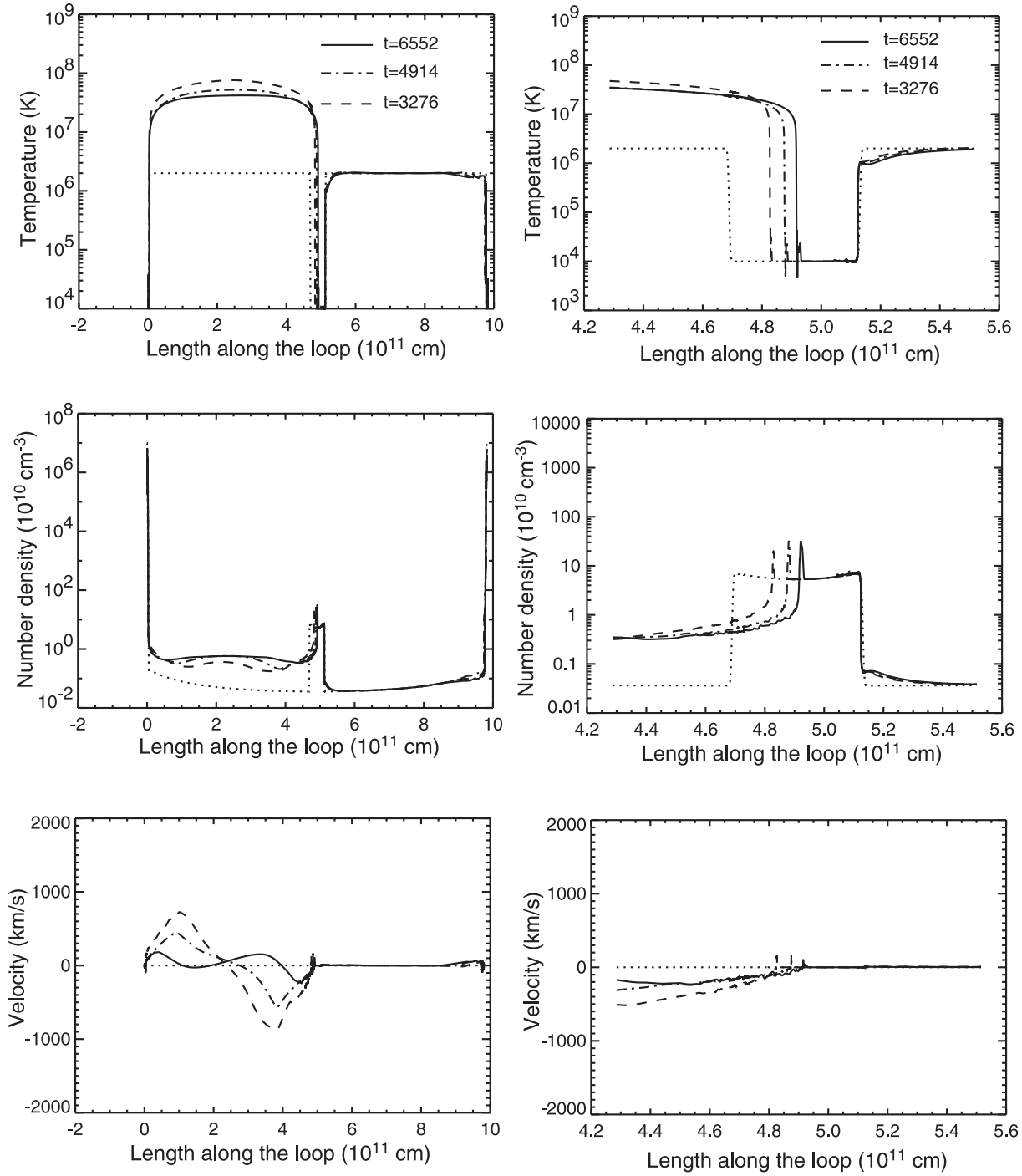

Fig. 6. Result for case A, t = 3276, 4914, and 6552 s.

4. Discussion

It should be noted that, as mentioned above, the actual magnetic geometry in YSOs is controversial. The scenario of flares involving the stellar accretion disk is not well-established, and is still to be proven.

To the best of our knowledge, so far the only observational evidence supporting the disk–star flare scenario is the long (> a few stellar radii) loop length inferred from spatially unresolved observations. For example, quasi-static analyses (van den Oord, Mewe 1989) of the decay phase of flares in YSOs often yield long loop length (e.g., Tsuboi et al. 2000). Shibata and Yokoyama (1999, 2002) have made a scaling law which relates the peak temperature and emission measure to the loop length and the magnetic field strength (and hence flare heating flux). They found the loop length to be about 10^{11} cm ($\sim$ 1 stellar radii) for several stellar and YSO flares.

On the other hand, based on a hydrodynamic model of a

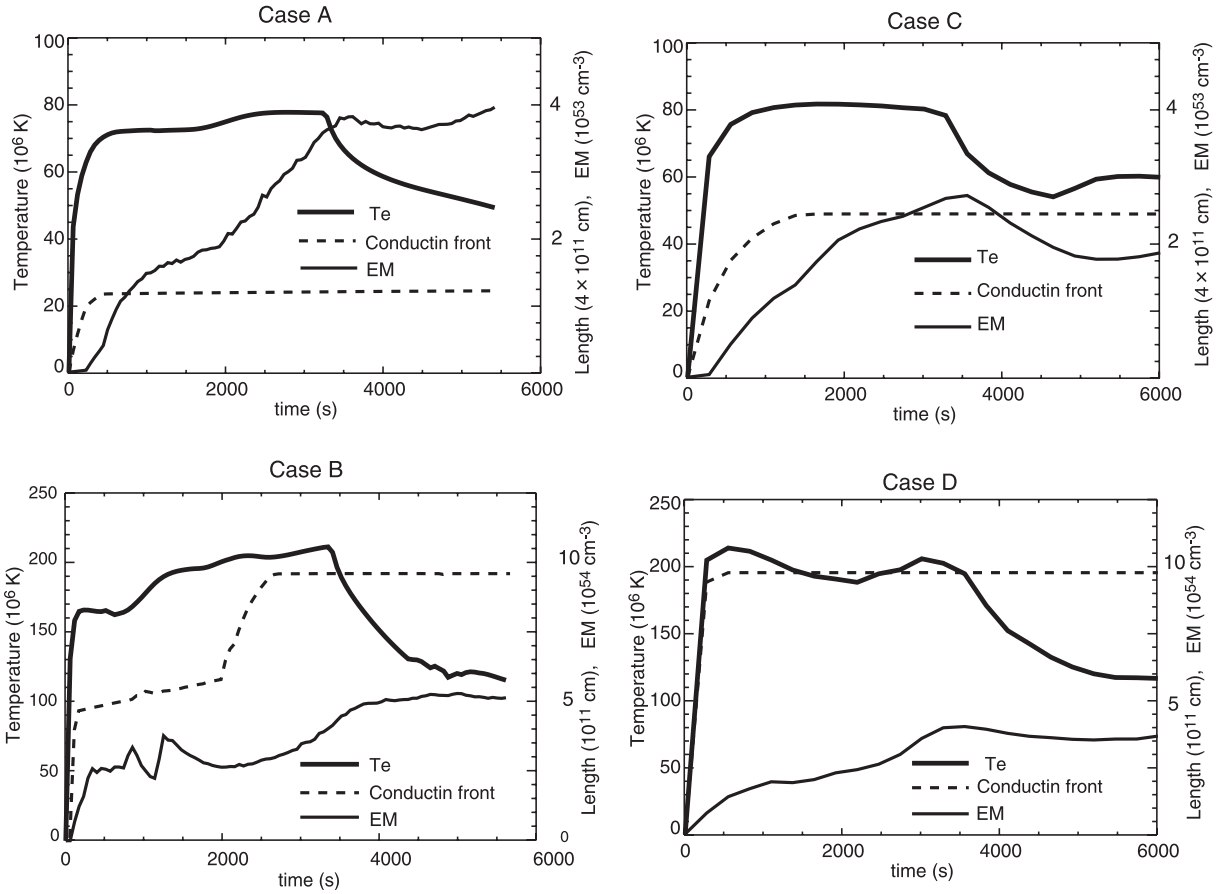

Fig. 7. Temporal variation of the maximum temperature in the loop (thick solid line), emission measure *EM* (thin solid line), and the distance between the two conduction fronts (dotted line).

decaying flare loop (Reale, Micela 1998), Favata et al. (2001) reanalyzed large flaring events on pre-main-sequence stars, and found that the size of the flaring regions is much smaller than stellar radii. Furthermore, Feigelson et al. (2003) showed that, using the Chandra observation of many pre-main-sequence stars in the Orion Nebula cluster, the X-ray luminosities have no apparent correlation to the existence of circumstellar disks inferred from the infrared excesses.

In order to find an observational signature which can be used as a diagnostic tool to test the disk–star flare scenario, we also performed simulations without a disk. The right panels in figure 7 show the temperature and emission measure evolution for the two cases without a disk. Case C/D (upper/lower right panel) is identical to case A/B, except for the absence of a disk; all the parameters are the same but there is no dense and cold disk in the initial corona. Although there are some differences in the temperature and emission measure evolutions, we could not find any clear signature of the existence of the disk. As discussed in the following subsections, the bulk properties of a flare loop, such as the temperature and emission measure, are determined by the flare heating flux and loop length, not by involvement of the disk. We plan to extend our model to a multi-loop model including a decay phase to find an observational signature of the existence/absence of a disk. However, we believe that it is still valuable to describe the basic processes in the single disk–star flare loops treated in this paper.

4.1. *What Determines the Flare Temperature?*

Since conduction cooling is dominant during the early phase, we expect the flare temperature to be determined by the balance between the flare heat flux F and the conduction cooling $\kappa_0 T^{7/2}/l$. Then, we can make a scaling law for the flare temperature,

$$T = \left(\frac{Fl}{\kappa_0}\right)^{2/7}, \tag{8}$$

where l is the half length of the flaring loop. In the followings, l is the half distance between the transition regions of the star and the disk in the initial condition, and hence $l \approx L/2$. This scaling law can be easily derived from the well-known RTV scaling law (Rosner et al. 1978).

Figure 11 shows the temperatures at the loop summit ($s = s_{\rm flr}$) in cases with different heat flux F. Other parameters, such as the loop length and heating duration, are fixed. The asterisks show the maximum temperature during the flare ($T_{\rm max}$). The diamonds show the temperature at the time when the conduction front reaches the chromosphere of the star and the disk ($T_{\rm CF}$), that is, when the length of the high temperature ($T > 10^7$ K) becomes larger than $2l = 4.6 \times 10^{11}$ cm, the initial distance between the transition regions of the star

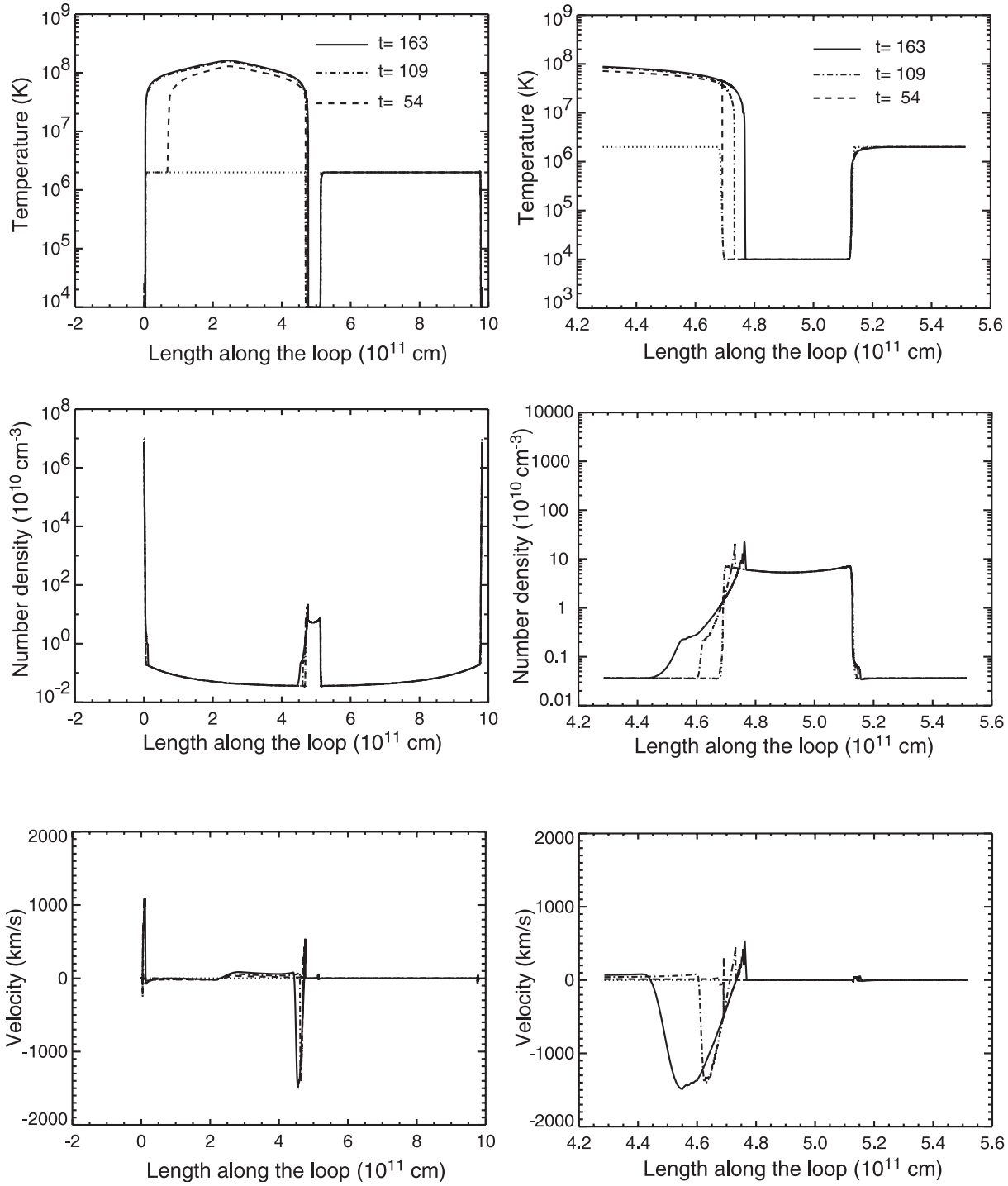

Fig. 8. Result for case B, $t = 54$, 109, and 163 s.

and the disk. At this time the evaporation flows have not yet reached the loop summit. The difference in $T_{\max}$ and $T_{\rm CF}$ is mainly due to the collision of evaporation flows, and the resultant temperature increase near the loop summit. The slight increases of temperature around $t = 1800$ s in case A and around $t = 800$ s in case B correspond to the collision of evaporation flows (figure 7). Since larger F causes stronger evaporation, $T_{\max} - T_{\rm CF}$ increases with the heat flux F. The solid line illustrates the calculated temperature given by equation (8). The simple scaling law (8) well explains the numerical result, though it gives slightly lower temperature in larger F cases.

Plotted in figure 12 are the same parameters as figure 11 in the cases with different loop length l. The heat flux F is fixed to $1.6 \times 10^{10}\,{\rm erg\,cm^{-2}\,s^{-1}}$ in these cases. Again the temperature given by the scaling law (8) is close to the numerical result. The large asterisks/diamonds in figures 11 and 12 indicate the

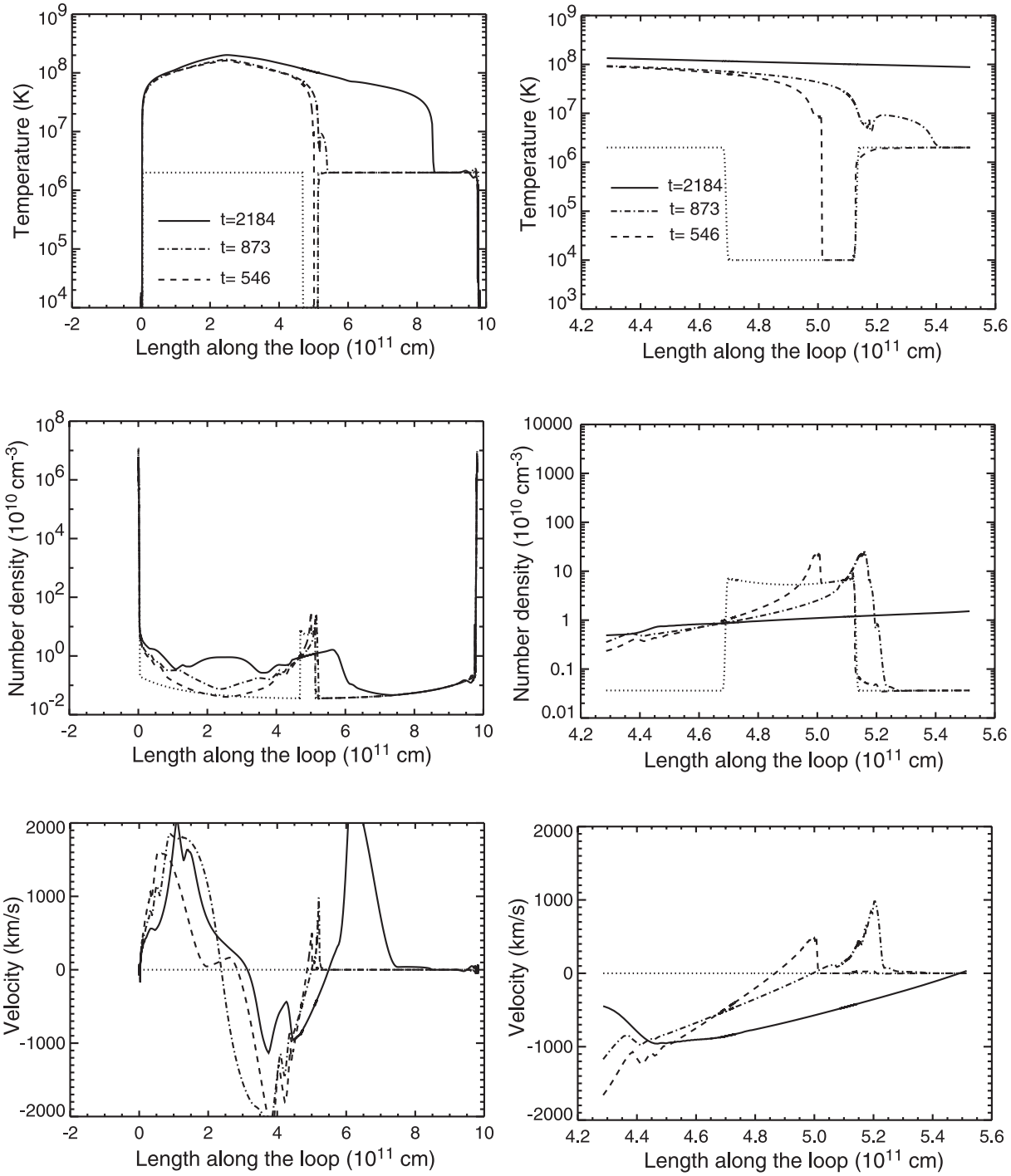

Fig. 9. Result for case B, t = 546, 873, and 2184 s.

cases in which the disk disappears.

4.2. *What is the Condition for Disk Disappearance?*

Our simulation result demonstrates that part of the accretion disk connected to the flare loops is evaporated and disappears if the heat flux is large enough, as pointed out by Isobe et al. (2001). We use "disappear" to refer to the situation in which all the initially cold and dense plasma of the disk is heated to the flare temperature ($> 10^7$ K) and spreads over the loop. Here we examine the condition for disappearance of the disk.

The disk disappears when the total mass carried by the evaporation flow is larger than the initial mass in the disk. If we neglect the radiative losses, the enthalpy flux of evaporation flow and the conductive flux balance (e.g., Shibata, Yokoyama 1999; Shimojo et al. 2001),

$$\kappa_0 T^{5/2} \frac{dT}{ds} \sim \frac{\kappa_0 T^{7/2}}{l} \sim \frac{\gamma}{\gamma - 1} p v_e \sim \frac{5}{2} \frac{R_g T}{\mu} \rho_e v_e, \qquad (9)$$

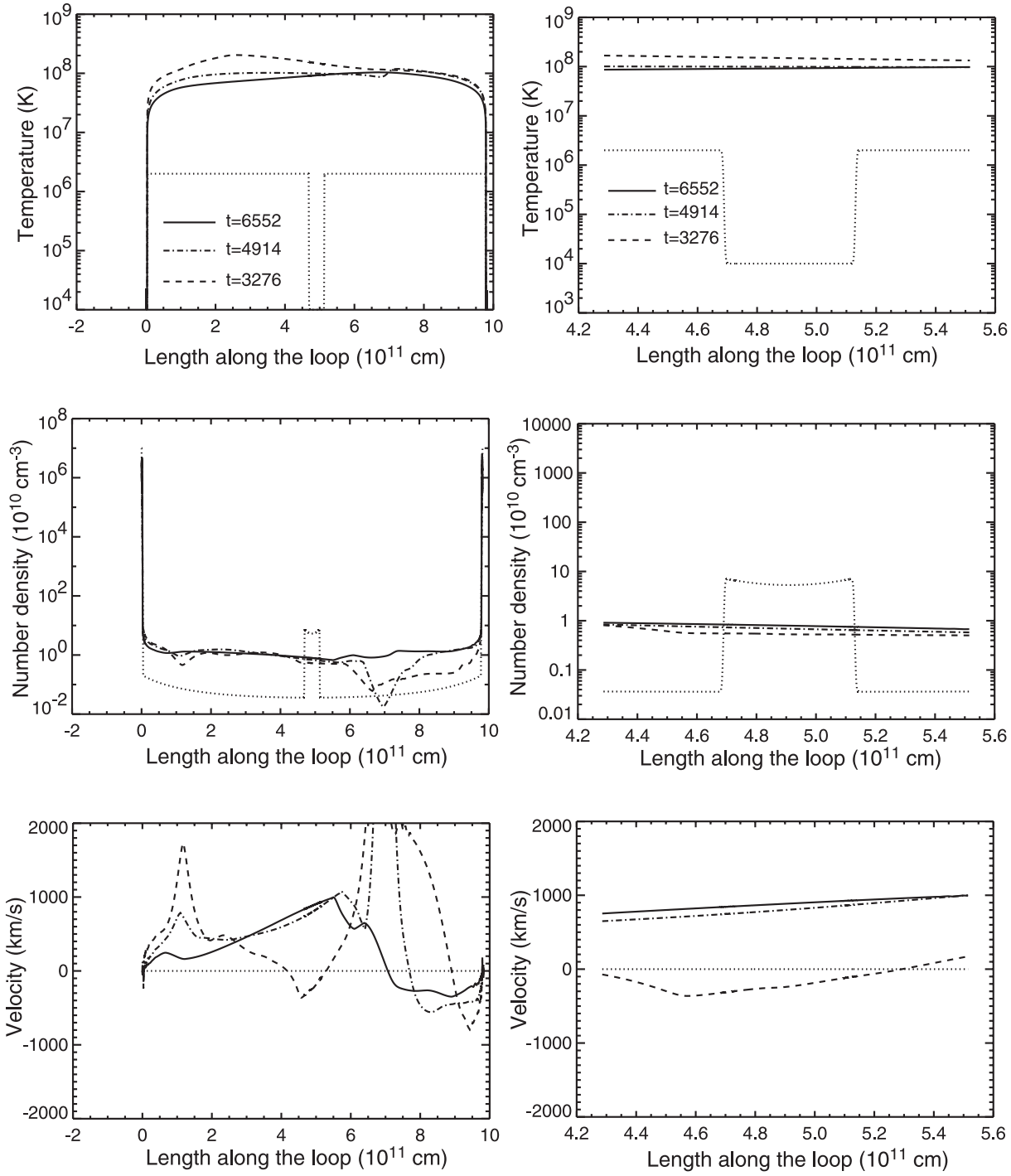

Fig. 10. Result for case B, t = 3276, 4914, and 6552 s.

where R_g is the gas constant, μ is the mean molecular mass, and v_e and $\rho_e v_e$ are the velocity and mass flux of the evaporation flow, respectively. The total mass carried by the evaporation flow for a flare duration time t_f is then written as $\rho_e v_e t_f$. Thus, the condition for a disappearance of the disk is given by

$$\rho_e v_e t_f > \rho_d H_d, \tag{10}$$

where ρ_d and H_d are the density and thickness of the accretion disk. From equations (9) and (10), we obtain the condition for disk disappearance:

$$\rho_e v_e t_f \sim \frac{2}{5}\frac{\mu\kappa_0 T^{7/2} t_f}{R_g T l} > \rho_d H_d \tag{11}$$

$$T^{5/2} > \frac{5 R_g l \rho_d H_d}{2\mu\kappa_0 t_f} \tag{12}$$

$$T > T_c = \left(\frac{5 R_g l \rho_d H_d}{2\mu\kappa_0 t_f}\right)^{2/5}. \tag{13}$$

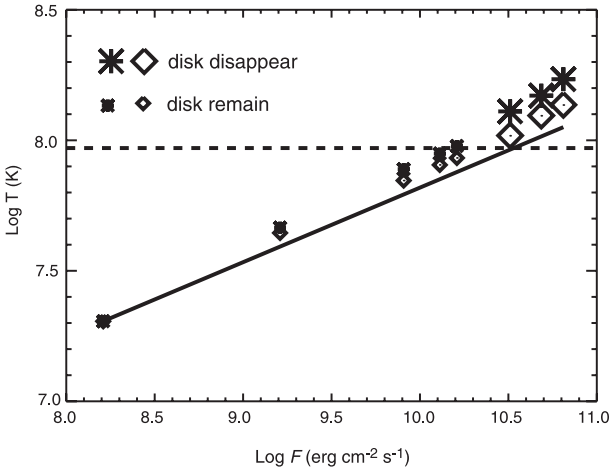

Fig. 11. Temperatures at the loop summit ($s = s_{\rm flr}$) in cases with different heat flux F. The diamonds show the temperature at the time when the conduction front reaches the chromosphere of the star and the disk ($T_{\rm CF}$). The asterisks show the maximum temperature during the flare ($T_{\rm max}$). The large symbols indicate the cases in which the disk disappears. The solid line shows $T = (Fl/\kappa_0)^{2/7}$, and the dashed line shows the critical temperature $T_{\rm c}$.

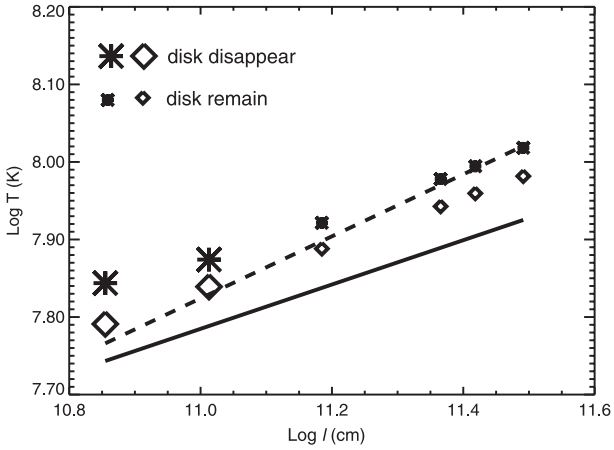

Fig. 12. Temperatures at the loop summit ($s = s_{\rm flr}$) in cases with different loop length l. The diamonds show the temperature at the time when the conduction front reaches the chromosphere of the star and the disk ($T_{\rm CF}$). The asterisks show the maximum temperature during the flare ($T_{\rm max}$). The large symbols indicate the cases in which the disk disappears. The solid line shows $(Fl/\kappa_0)^{2/7}$, and the dashed line shows the critical temperature $T_{\rm c}$.

Namely, the disk disappears if the flare temperature is higher than a critical temperature $T_{\rm c}$ determined by the loop length, flare duration, and column density of the disk. Substituting typical values in the present simulations,

$$T_{\rm c} = 9.3 \times 10^7 \left(\frac{l}{2.7 \times 10^{11}\,{\rm cm}}\right)\left(\frac{\rho_{\rm d}}{1.0 \times 10^{-13}\,{\rm g\,cm^{-3}}}\right) \times \left(\frac{H_{\rm d}}{4.5 \times 10^5\,{\rm cm}}\right)\left(\frac{t_{\rm f}}{3276\,{\rm s}}\right)^{} {\rm K}. \quad (14)$$

$T_{\rm c}$ is shown by the dashed lines in figures 11 and 12. The large asterisks/diamonds indicate the cases in which disk disappearance occurs. Thus, our results are in agreement with the condition that the disk disappears if the maximum temperature is larger than $T_{\rm c}$.

4.3. Expected X-Ray Spectrum

Figure 13 shows the emission measure $EM(T)$ as a function of temperature in case B, which is averaged over $t = 0$–8190 s. The unit of emission measure is arbitrary. Note that the maximum temperature is larger than 20 keV. Although the observed X-ray spectra of flares are often reproduced by an optically-thin thermal plasma model with one or two temperatures, the actual flare spectrum must be a superposition of the emission from the plasma with a continuous differential emission measure, such as shown in figure 13. We synthesize the X-ray spectrum expected when we *observe* this flare by the gas-imaging spectrometer (GIS) of ASCA. We assume the thin thermal plasma model and fold it through the instrumental response of GIS.

Since we used a one-dimensional model, the volume of the flare loop V and the total emission measure $EM = n^2\,V$ is arbitrary. If the aspect ratio (radius/length) of the loop is 0.1, $V = 0.01 \times \pi(2L)^3 = 3 \times 10^{34}\,{\rm cm^3}$. Then the total emission measure is $\sim 3 \times 10^{54}\,{\rm cm^{-3}}$, because $n \sim 10^{10}\,{\rm cm^{-3}}$ in the

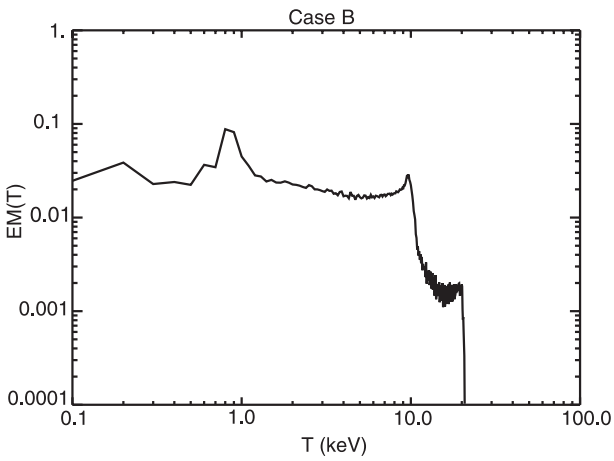

Fig. 13. Temporal average of the emission measure in case B during $t = 0$–8190 s.

flare loop. For a comparison we synthesize the spectra for the two cases of $EM = 3 \times 10^{54}\,{\rm cm^{-3}}$ and $EM = 3 \times 10^{56}\,{\rm cm^{-3}}$. Keeping in mind the ρ Oph cloud for an example, we assume the distance to the flare is 160 pc. The exposure time is 8190 s.

Figure 14 shows the synthesized spectrum for the case of $EM = 3 \times 10^{54}\,{\rm cm^{-3}}$. The solid lines in the upper and lower panels show the best-fit one-temperature model and two-temperature model, respectively. Each component of the two-temperature model is also shown by the dashed lines. The residuals from the model are shown in the lower part in each panel. For the one-temperature model, the best-fit parameters are $kT = 3.6^{+0.5}_{-0.4}$ keV and $EM = 2.8^{+0.2}_{-0.1} \times 10^{54}\,{\rm cm^{-3}}$, and reduced $\chi^2 = 1.49$. For the two-temperature model, the best-fit parameters are $kT_1 = 0.73^{+0.27}_{-0.18}$ keV, $EM_1 = 4.0^{+1.2}_{-1.1} \times 10^{53}\,{\rm cm^{-3}}$, $kT_2 = 5.8^{+2.2}_{-1.2}$ keV, $EM_2 = 2.3^{+0.2}_{-0.2} \times 10^{54}\,{\rm cm^{-3}}$, and reduced $\chi^2 = 0.675$. The one-temperature model yields large residuals

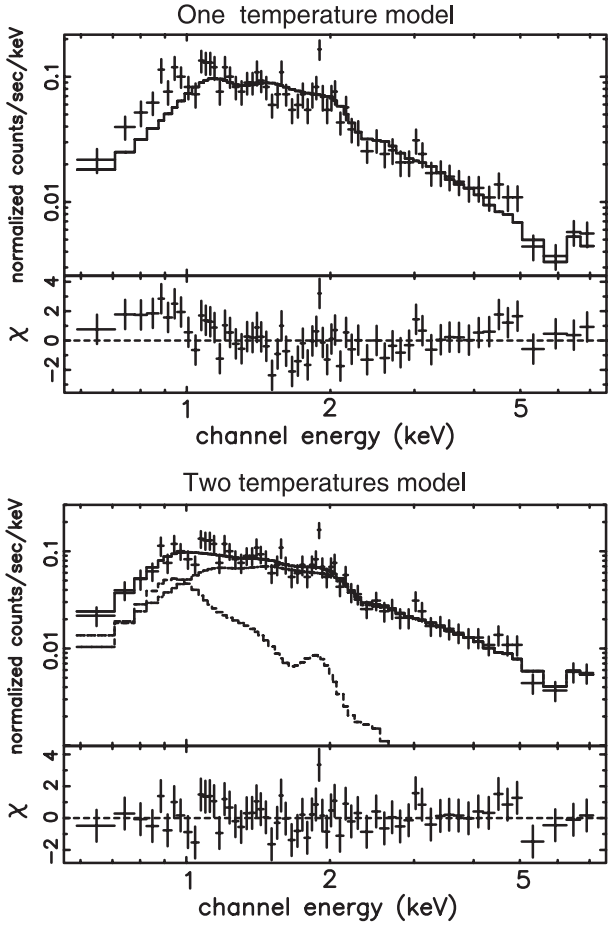

Fig. 14. Synthesized X-ray spectrum for case B. Total EM is assumed to be $3 \times 10^{54}\,\mathrm{cm}^{-3}$. The solid lines in the upper and lower panels show the best-fit one-temperature model and two-temperature model respectively. Each component of the two-temperature model is also shown by the dashed lines. The residuals from the model are shown in the lower part in each panel.

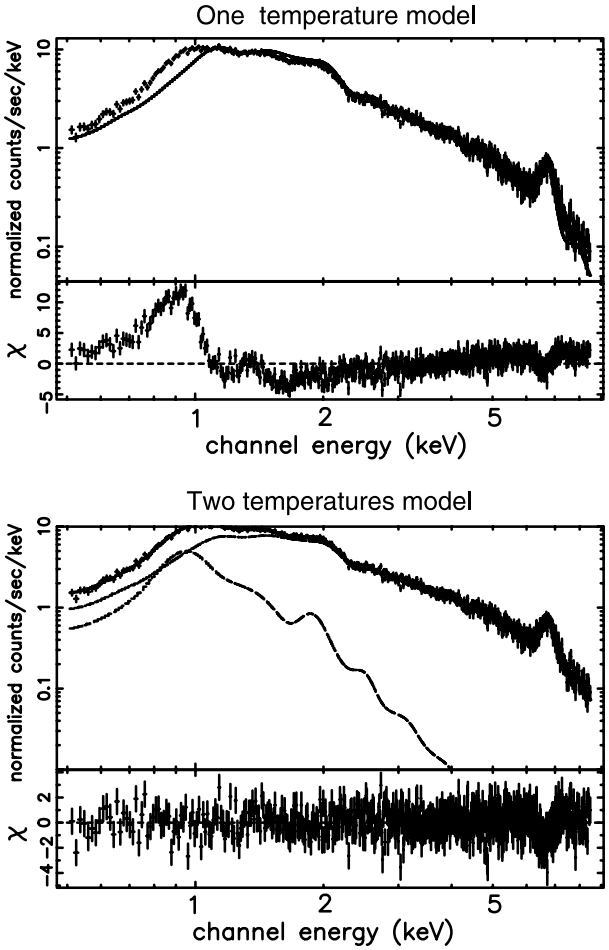

Fig. 15. Synthesized X-ray spectrum for case B, with total $EM = 3 \times 10^{56}\,\mathrm{cm}^{-3}$. The solid lines in the upper and lower panels show the best-fit one-temperature model and two-temperature model respectively. Each component of the two-temperature model is also shown by the dashed lines. The residuals from the model are shown in the lower part in each panel.

at $kT < 1\,\mathrm{keV}$. On the other hand, the two-temperature model well reproduces the synthesized spectrum.

The spectrum for the case of $EM = 3 \times 10^{56}\,\mathrm{cm}^{-3}$ is shown in figure 15 with the best-fit one- and two-temperature models. Because of good statistics, an emission line near 6.7 keV is clearly seen. The best-fit parameters are $kT = 3.7\,\mathrm{keV}$ and $EM = 3.08 \times 10^{56}\,\mathrm{cm}^{-3}$ for the one-temperature model, which is obviously inadequate (reduced $\chi^2 = 6.06$). For the two-temperature model, $kT_1 = 0.78^{+0.02}_{-0.02}\,\mathrm{keV}$, $EM_1 = 3.6^{+0.1}_{-0.2} \times 10^{55}\,\mathrm{cm}^{-3}$, $kT_2 = 5.1^{+0.1}_{-0.1}\,\mathrm{keV}$, $EM_2 = 2.6^{+0.1}_{-0.1} \times 10^{56}\,\mathrm{cm}^{-3}$, and reduced $\chi^2 = 1.18$. This reasonably reproduces the synthesized spectrum, even near $kT = 10\,\mathrm{keV}$.

The above results demonstrate that even the maximum temperature is as high as 20 keV, the synthesized spectrum can be reasonably fitted by the two-temperature model of $kT = 0.7$–$0.8\,\mathrm{keV}$ and 5–6 keV. This indicates that the temperature derived from observed spectra is several factors smaller than the maximum temperature. In other words, the scaling law [equation (8)] gives a temperature several factors higher than the observed one. This is quantitatively consistent with previous spectral fittings based on a hydrostatic model (Maggio, Peres 1996; Favata et al. 2000), though our result seems to yield a lower fitted temperature.

4.4. *Concluding Remarks*

In this paper we have presented the hydrodynamic modeling of a flare loop connecting the central star and the disk, taking into account the heat conduction and evaporation of the disk for the first time. We have found that in some conditions the plasma in the accretion disk connected to the flare loop is heated to the flare temperature and spreads over the loop. The sudden heating of the disk matter by a flare may be a candidate of high-energy processes in protoplanetary nebula, which are implied by meteoritic evidence (e.g. Feigelson et al. 2002).

The X-ray spectrum expected when we observe the simulation result was calculated while considering the instrumental response of ASCA/GIS. Fitting of the synthesized spectrum by one- or two-temperature models yields several factors of lower temperature than the maximum temperature of the simulation result. This indicates that the temperature derived from the

observed spectra is several factors smaller than the maximum temperature.

We could not find in our present simulations any clear signature which can be used as a diagnostic tool to test the disk–star flare scenario in spatially unresolved observations. We plan to carry out a further parameter survey and modeling of the decay phase in the future. In particular, on the basis of the magnetic reconnection model, continuous heating of a flare occurs by successive reconnection in different loops, which can not be treated by a one-dimensional approach. A pseudo two-dimensional approach, such as done by Hori et al. (1997) and Reeves and Warren (2002) for solar flares, is necessary for a realistic modeling of the temporal evolution of the temperature and emission measure.

This work was supported by Japan Science and Technology Cooperation (ACT-JST) and also by Giants-in-Aid for Scientific Research (14540226) from the Japanese Ministry of Education, Culture, Sports, Science and Technology. H.I. is supported by the Research Fellowship of the Japan Society for the Promotion of Science for Young Scientists. A part of this work was carried out by using the computer facilities at the Astronomical Data Analysis Center of the National Astronomical Observatory of Japan, which is an inter-university research institute of astronomy operated by the Japanese Ministry of Education, Culture, Sports, Science and Technology.

References

Choe, G. S., & Lee, L. C. 1992, Sol. Phys., 138, 291
Favata, F., Micela, G., & Reale, F. 2001, A&A, 375, 485
Favata, F., Reale, F., Micela, G., Sciortino, S., Maggio, A., & Matsumoto, H. 2000, A&A, 353, 987
Feigelson, E. D., Gaffney, J. A., III, Garmire, G., Hillenbrand, L. A., & Townsley, L. 2003, ApJ, 584, 911
Feigelson, E. D., Garmire, G. P., & Pravdo, S. H. 2002, ApJ, 572, 335
Feigelson, E. D., & Montmerle, T. 1999, ARA&A, 37, 363
Grosso, N., Montmerle, T., Feigelson, E. D., André, P., Casanova, S., & Gregorio-Hetem, J. 1997, Nature, 387, 56
Hayashi, M. R., Shibata, K., & Matsumoto, R. 1996, ApJ, 468, L37
Hirsch, C. 1988, Numerical Computation of Internal and External Flows, Vol. 1 (New York: Wiley), 476
Hori, K., Yokoyama, T., Kosugi, T., & Shibata, K. 1997, ApJ, 489, 426
Isobe, H., Yokoyama, T., & Shibata, K. 2001, J. Korean Astron. Soc., 34, S337
Kamata, Y., Koyama, K., Tsuboi, Y., & Yamauchi, S. 1997, PASJ, 49, 461
Koyama, K., Hamaguchi, K., Ueno, S., Kobayashi, N., & Feigelson, E. D. 1996, PASJ, 48, L87
Koyama, K., Maeda, Y., Ozaki, M., Ueno, S., Kamata, Y., Tawara, Y., Skinner, S., & Yamauchi, S. 1994, PASJ, 46, L125
Maggio, A., & Peres, G. 1996, A&A, 306, 563
Montmerle, T., Grosso, N., Tsuboi, Y., & Koyama, K. 2000, ApJ, 532, 1097
Ozawa, H., Nagase, F., Ueda, Y., Dotani, T., & Ishida, M. 1999, ApJ, 523, L81
Reale, F., Betta, R., Peres, G., Serio, S., & McTiernan, J. 1997, A&A, 325, 782
Reale, F., & Micela, G. 1998, A&A, 334, 1028
Reeves, K. K., & Warren, H. P. 2002, ApJ, 578, 590
Rosner, R., Tucker, W. H., & Vaiana, G. S. 1978, ApJ, 220, 643
Rubin, E. L., & Burkstein, S. Z. 1967, J. Comput. Phys., 2, 178
Shibata, K., & Yokoyama, T. 1999, ApJ, 526, L49
Shibata, K., & Yokoyama, T. 2002, ApJ, 577, 422
Shimojo, M., Shibata, K., Yokoyama, T., & Hori, K. 2001, ApJ, 550, 1051
Shu, F. H., Adams, F. C., & Lizano, S. 1987, ARA&A, 25, 23
Spitzer, L. 1962, Physics of Fully Ionized Gases (New York: Interscience)
Tsuboi, Y., Imanishi, K., Koyama, K., Grosso, N., & Montmerle, T. 2000, ApJ, 532, 1089
van den Oord, G. H. J., & Mewe, R. 1989, A&A, 213, 245
Yokoyama, T., & Shibata, K. 1998, ApJ, 494, L113
Yokoyama, T., & Shibata, K. 2001, APJ, 549, 1160